Supporting information

Nanoscale Heat Transport Analysis by Scanning Thermal Microscopy: from calibration to High-Resolution Measurements

Liliana Vera-Londono[1], Alejandra Ruiz-Clavijo[1], Jaime Andres Perez-Taborda[1,2], and Marisol Martin-Gonzalez[1]

1 Instituto de Micro y Nanotecnología, IMN-CNM, CSIC (CEI UAM+CSIC) Isaac Newton, 8, E-28760, Tres Cantos, Madrid, Spain

2 Universidad Nacional de Colombia Sede De La Paz, Escuela de pregrados-Dirección Académica -Vicerrectoría, Grupo de Nanoestructuras y Física Aplicada (NANOUPAR), Km 9 vía Valledupar La Paz, La Paz 202010, Colombia

S.I.1. Fourier Law applied to probe temperature distribution:

The heat equation solved in the Fourier space is presented in equation S.I.1:

$$\frac{d^2T_{2\omega,P}}{dx^2} - \left(\frac{2i\omega}{\alpha_P} + \frac{hp_P}{\lambda_P A_P}\right)T_{2\omega,P} + \frac{\rho I_0^2}{2\lambda_P A_P A_M} = 0 \quad \text{(S.I.1)}$$

, where α_P, λ_P and A_P represent the probe thermal diffusivity, thermal conductivity total cross-sectional area, respectively; h *is* the effective convective heat transfer coefficient in the air; p is the probe perimeter; ρ is the electrical resistivity and A_M is the cross-sectional area of the metallic film of the heater element. If $\omega \to 0$, the equations when the probe is heated by AC should be simplified as if it were subjected to DC heating, with no transient contribution. If the heat flux only takes place at the tip apex, the metal pads in the tip made of NiCr can be considered as thermal sinks, and then temperature variation at this junction can be neglected. Based on these considerations, the heat flux when the probe is in contact with the sample can be expressed as:

$$-\lambda_P A_P \left.\frac{dT_{2\omega,P}}{dx}\right|_{x=L} = \frac{T_{2\omega,P}|_{x=L}}{R_{eq}} \quad \text{(S.I.2)}$$

, where R_{eq} is the equivalent thermal resistance, which is the result of the thermal resistances in series from both the thermal contact resistance R_c and the thermal sample resistance R_s. The analytical solution for tip temperature variation at 2ω is found by solving the transient fin equation as in [1-3], applying the boundary conditions for both cases out of contact and in contact with the sample. And the heat transfer balance for the sample is:

$$Q_{tip-sample} = \frac{(T_{tip} - T_0)}{R_{eq}} = \frac{(T_s - T_0)}{R_s} \quad \text{(S.I.3)}$$

, where T_{tip}, T_s, and T_0, are the tip temperature, the sample temperature, and the room temperature, respectively.

S.I.2. Two-fold symmetry at V-shaped thermistor probes:

The energy balance equation accounts for half of the heat transfer rate between the probe and the sample. If the heat transfer between the tip and the sample occurs only at the tip of the probe (x=L) it enables an analytical solution to the heat transfer model as:

$$-\kappa A \frac{dT}{dx}\Big|_{x=L} = \frac{Q_s}{2} \quad \text{(S.I.4)}$$

, where κ is the thermal conductivity, and Q_s is the heat transfer rate.

S.I.3. RMS for the input data of voltage and current:

The thermo-resistive probes heated by alternating voltages have a probe temperature profile rise with a contribution of both direct (DC) and alternating current (AC). The electrical current passing through one of the probe legs (I/2) is calculated with the Root-Mean-Squared Voltage (V_{rms}), which is the equivalent voltage value as if the resistor was heated by a DC power. In the experimental case presented in the paper, the selected voltages values were a first voltage to the peak of 4 V (V_{pk}), which is equal to 2.8 V (V_{rms}), and the second voltage applied to the second probe with a voltage to the peak of 6 V (V_{pk}), which is equivalent to 4.24 V (V_{rms}). See the expressions in the equations S.I.5. to S.I.7.

The input voltage on the bridge should be carefully selected so as not to overload the lock-in system. The voltage was increased from volt to volt until reaching the desired value. Then, the pre-amplifier gain was increased progressively from 5x to 50x. The final gain value is selected depending on the 3ω voltage signal. Thus, if $V_{3\omega}$ was higher than 100 mV, we used a lower pre-amplifier gain value to avoid any saturation in the signal. The higher the voltages at the entrance, the larger $V_{3\omega}$ signal, but the higher the risk of damaging the tip due to its sensitive electrical characteristics.

The power supplier heat-up the probe with a sinusoidal voltage, whose instantaneous voltage υ(t) and amplitude voltage to peak (V_{pk}) are expressed as:

$$\upsilon(t) = V_{pk}\cos(\omega t + \phi) \quad \text{(S.I.5)}$$

$$V_{pk} = \frac{V_{pp}}{2} \quad \text{(S.I.6)}$$

and, where V_{pp} is the peak-to-peak voltage.

The RMS voltage value (V_{rms}) of the sinusoidal waveform:

$$V_{rms} = \frac{V_{pk}}{\sqrt{2}} = 0.707 \cdot V_{pk} \qquad \text{(S.I.7)}$$

S.I.4. Wheatstone bridge and experiment set-up

In Figure S.I.1, the photos of the lab-made Wheatstone bridge used in our experiment can be observed (top and lateral view). Using a current supply instead of the voltage supply can be a better option for data acquisition since it can reduce the noise signal by parasitic currents and voltage drop. We modified the voltage-generated signal by adding an electrical resistance to the bridge entrance, inducing a current signal instead of a voltage one. About the use of current and voltage signals, Dames C. and Chen G.[4] discussed the importance of using a correction factor for thermal measurements when assuming AC sources while carrying out experiments with a voltage source.

In our experiment, we determined the current across the probe by Faraday's Law, and we corroborated our results with the Multisim simulator for the Wheatstone bridge. As is shown in Figure S.I.2.a., the Wheatstone bridge connection has been modified with a limiter resistance R_{lim} ~ 1000 Ω in the bridge entrance, which may cause the voltage entrance to act as a current source type. The limiter resistance can protect the probe from higher currents that could damage the Pd resistive film. The values used in the present work are limiter resistances of 1000 Ω and 30000 Ω, in a parallel configuration, with a total value of R_{lim} ~ 968 Ω. Two fixed resistances with 1000 Ω each of them in R1 and R2. In the circuit simulation, Figure S.2.b and S.2.c, we used R_{lim1}= 995 instead of 1000 Ω, considering the tolerance of the resistance of 5%. The resistances R_1 and R_2 in the bridge have the same tolerance value of 5%, but we add some resistance to the cables and connectors. The final value of resistance that we used in the circuit simulation is 1000 Ω in each resistance of R_1 and R_2. The potentiometer or variable resistance R_{Vc} has a maximum value of 10 kΩ for coarse adjustment in series with resistance for fine adjustment of 100 Ω (R_{Vf}).

Before performing any scan, the bridge is calibrated to zero. This means that the variable resistances, the coarse and the fine-tune resistances, are fixed to the same value as the electrical probe resistance. The probes exhibit different resistances, the first probe had 374 Ω, and the second probe had 366 Ω. The voltage drop between a and b points in the bridge will be zero, and the electrical currents determined in each case are approximately 0.8 mA and 1.28 mA (see Figures S.I.2.b. and S.I.2.c.).

After feeding the circuit with a power supply of 4 V_{pk}, Vin was measured as 1.17 Volts, and the current amplitude in one leg of the probe is ~0.8 mA. When the voltage was increased to 6 V_{pk}, the V_{in} was measured as 1.75 Volts, and in that case, the current passing through the probe was ~1.28 mA. These data are presented in Table S.I.1, where column a) has the resistance values of the probes. The voltage value corresponding to one peak in column b). The root-mean-square (RMS) voltage of the sinusoidal signal is presented in column c). The voltage value after limiter resistance was measured by a hand-multimeter while the experiment was performed, see column d). Also, the values were monitored by a table multimeter during the analysis of signal stability and noise analysis in the Wheatstone bridge. These values are in column e). Columns f), g), ad h) are the resistance in series and parallel that compounds the bridge. The total current passing

through the bridge and half of the current passing through one leg of the probe were respectively determined and appear in i) and g) columns, respectively.

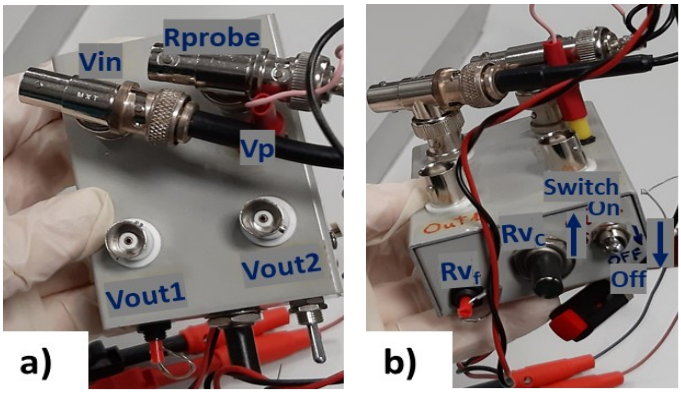

Figure S.I.1: Home-made Wheatstone bridge. In a) the top view of the Wheatstone bridge, where it can be seen the BNC connectors to V_{in} (for power supply) and V_p (to monitor the entrance voltage in V_{rms} after the limiter resistance, R_{probe} (for probe connection), V_{out1} and V_{out2} to control the out-voltage difference in the bridge, the V_a and V_b of the Wheatstone bridge scheme. In b) Rv_f is the variable fine-tune resistance of the potentiometer. R_{Vc} is the variable resistance with coarse adjustment; switch on/off to close/open the circuit.

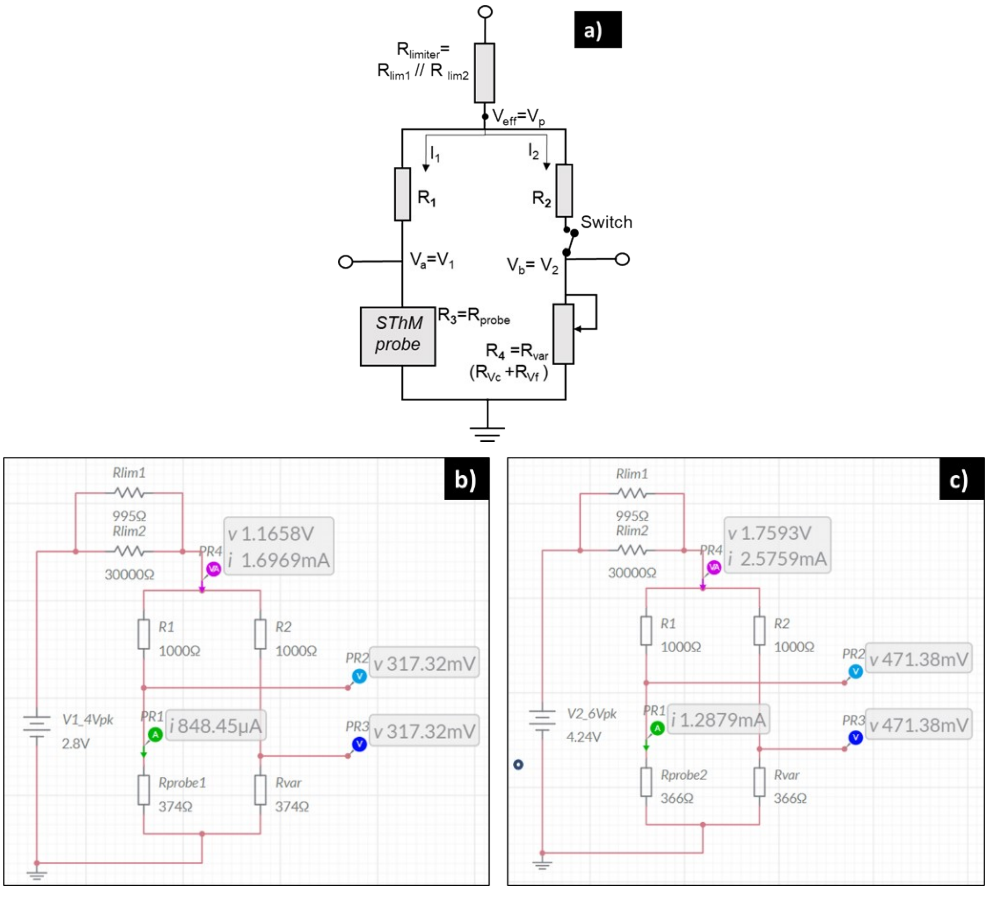

Figure S.I.2: Scheme of the lab-built Wheatstone bridge in a). In b) and c), Wheatstone bridge circuit designed in Multisim simulator, where the electrical current in the thermal probe can be determined. In b) V_{in}=4V_{pk} and I= 0.8 mA. In c) V_{in}= 6 V_{pk} and I= 1.29 mA.

Table S.I.1: Data used to determine the electrical current in the probe.

a)	b)	c)	d)	e)	f)	g)	h)	i)	j)
R_{probe}	V_{in}	V_{rms}	V_{in_probe} (RMS)	Volt. drop (oscilloscope)	R_a	R_b	R_{total}	I_{total}	I_1
R_1 R_2	V_{pk}	$V_{pk} \cdot 0.7$	Measured after limiter resistance	(Limiter Resisance~1k Ω) Lissajous analysis	R_a= (R_1 + R_{probe}) R_1=1kΩ	R_b= (R_2+R_{var}) R_{var}= R_{probe} R_2=1kΩ	R_a = R_b, R_{tot}= R_a/2	V_{in_probe} / R_{tot}	I_1 = I_{total}/2
Units	V	V	V	V	Ω	Ω	Ω	A	mA
374Ω	4	2.828	1.165	1.1701	1377	1374	687	0.00169	0.84
366 Ω	6	4.243	1.747	1.7506	1366	1366	683	0.00255	1.28

The experimental setup for probe calibration in vacuum and atmospheric conditions is shown in photos in the Figures S.I.3.a. and S.I.3.b., respectively. And the instrumentation for probe connection in Figures S.I.4.a. to S.I.4.e.

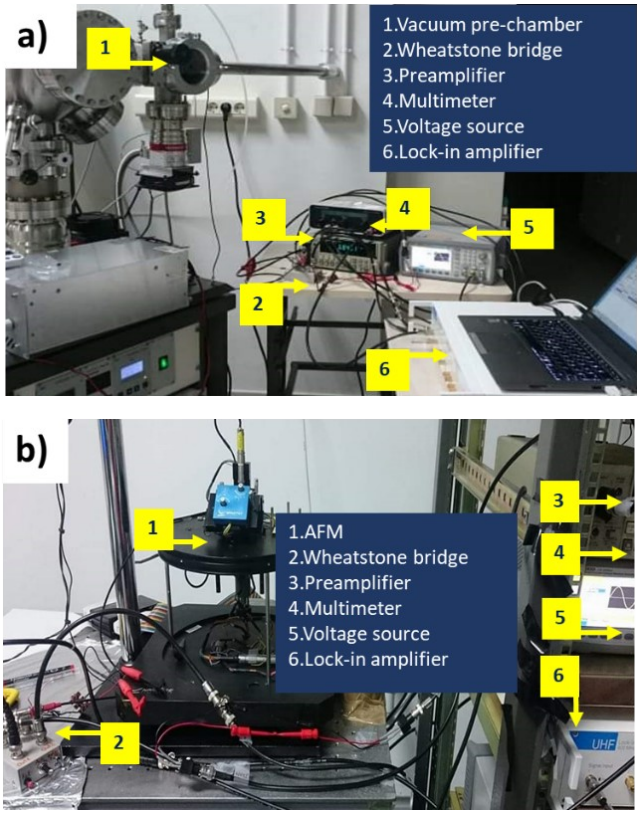

Figure S.I.3: Equipment used in SThM measurements. In a) the experimental setup used to calibrate the SThM probe under vacuum conditions (~ 6.3×10^{-6} mbar). In b) the experiment setup for calibration under atmospheric conditions.

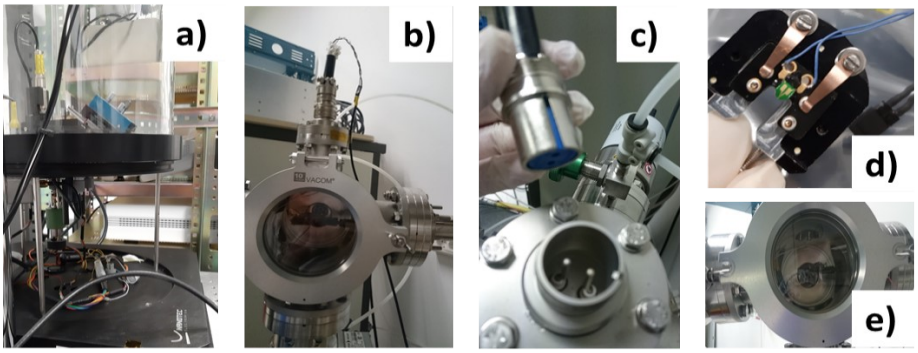

Figure S.I.4: SThM instrumentation and probe protection. In a) AFM under atmospheric conditions. In b) the equipment used for the probe's calibration in a vacuum system. In c) the protection for the probe's connection in the vacuum pre-chamber. In d) the cantilever holder. In e) the probe's location using the cantilever holder.

S.I.5. Effective medium theory

In the expression (S.I.8), the contribution of thermal conductance between the interfaces is neglected since the thermal resistance of the interfaces is smaller than the thermal resistance in the pores themselves. In this case, the porous can be treated as a homogeneous material along with the material solid membrane. Thus, it was assumed that thermal conductivity measurements determined after the cross-calibration method—in the case of porous structures, correspond to a composite thermal coefficient κ_c, which is a contribution of both components, the solid membrane and the pores filled with air. The composite thermal conductivity approach to the effective thermal conductivity from the effective medium theory , $\kappa_c = (x)\kappa_{air} + (1-x)\kappa_s$, where $\kappa_c$is the composite effective thermal conductivity, x is the areal packing density or porosity, κ_{air} is the thermal conductivity of the air, and κ_c is the sample´s thermal conductivity value, to be determined after applying this parallel model of EMT, $\frac{\kappa_c - (x)\kappa_{air}}{(1-x)} = \kappa_s$.

The Effective medium theory (EMT) is applied to the porous structure, in which the κ_c is composed of the thermal conductivity of the sample κ_s and the thermal conductivity of air κ_{air} through the porosity channels:

$$\kappa_c = (x)\kappa_{air} + (1-x)\kappa_s \qquad \text{(S.I.8)}$$

, where x is the porosity and the thermal conductivity of the air is $\kappa_{air} =$ 0.026 $W \cdot m^{-1} \cdot K^{-1}$. The data on effective thermal conductivity in silicon germanium samples are found in Table S.I.2.

Table S.I.2: Effective medium theory applied to porous structures. The porosity used in the calculations was taken from ref. [5].

Nanostructure/ ϕ_{pore}**(nm)**	ϕ_{pore}**(nm)**	$(1-x)$	κ_c **W/(m*K)**	κ_{EMT} **W/(m*K)**
a) AAO 1D	24	0.86	1.12 ± 0.07	1.29 ± 0.10
b) SiGe	20	0.97	0.56 ± 0.08	0.58 ± 0.12
c) SiGe	137	0.95	0.91 ± 0.10	0.95 ± 0.13
d) SiGe	294	0.7	0.99 ± 0.10	1.40 ± 0.13

The error was taken as the deviation of thermal conductivity measurements from the highest to lowest value of thermal voltage, or the lowest and highest thermal conductivity limits, corresponding to each thermal voltage limit. The error of the technique has been estimated in ref. [6] to be between 10 % and 15 %. The error of κ corresponds to the statistical deviation using different regions of the scanned sample. This deviation includes the highest value and the lowest thermal voltage value, or in other words, the lowest and highest thermal conductivity limits.

S.I.6. COMSOL simulation of SThM measurements in silver selenide film

To simulate the heating of the SThM probe over the sample, we used the circular Gaussian heat source and the heat transfer module of COMSOL (Figure S.I.5). To perform the simulation, we introduce the real thickness of the film, and we variate the possible thermal conductivity values, to find a common point of thermal resistance. This was done similarly for SiGe film using Wollaston probe [5]. The curves of thermal resistance *vs*. thermal conductivity obtained after the COMSOL simulation and experiments are presented in Figure S.I.6.

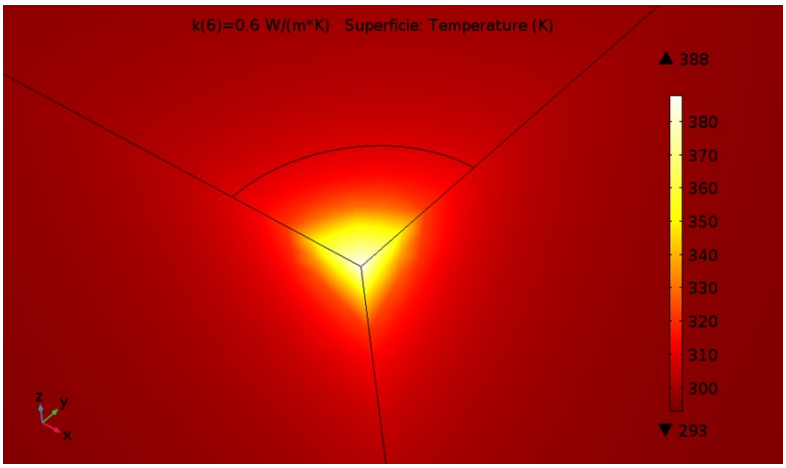

Figure S.I.5: COMSOL simulation of heating a silver selenide sample with an SThM probe.

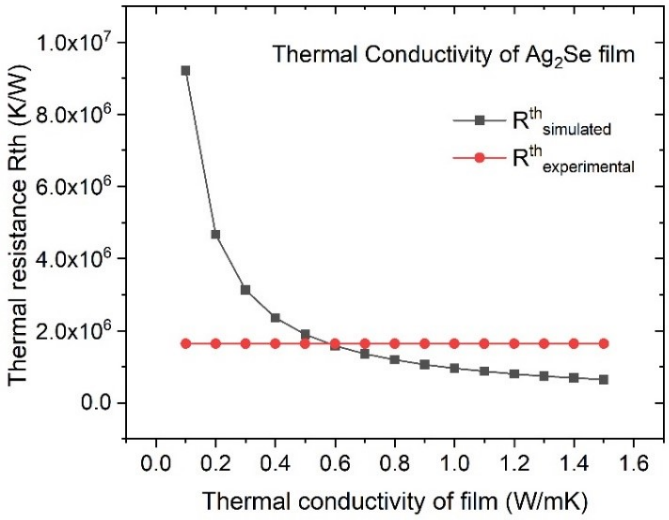

Figure S.I.6: In the graph, thermal resistance, simulated and experimental values, are cross at the point when thermal conductivity is around 0.6 $W \cdot m^{-1} \cdot K^{-1}$, which is very near to the value that we obtained by the experiments and analysis of the heat transfer model.

S.I.7. Thermal conductivity values of thermoelectric films: literature and measured

In Table S.I.3 is possible to observe and compare the thermal conductivity values from literature and the values determined in this work for some thermoelectric films.

Table S.I.3: Thermal conductivity reported for thermoelectric films and bulks samples obtained from the literature and the reported values in this work.

Thermoelectric films	Author and year of publication	Total thermal conductivity κ	Reference
Bi_2Te_3	This work (2021) ($\perp$ c-axis of the film and perpendicular to the substrate plane)	0.93	Reported here
	Kurokawa, T., et al. (2020) ($\parallel$ c-axis)	1.1	[7]
	Manzano, C.V, et al. (2016) ($\perp$ c-axis) / ($\parallel$ c-axis)	2.4 / 1.2	[8]
	Goncalves, L. M., et al. (2010) ($\perp$ c-axis)	1.3	[9]
	Obara, H., et al. (2009) ($\perp$ c-axis) / ($\parallel$ c-axis)	0.95 / 0.34	[10]
	Fleurial, J. P., et al. (1988) Single crystals	2 to 3.3	[11]

	Goldsmid, H. J. (1956) Bulk ($\perp$ c-axis)	1.87	[12]
Cu_2Se	This work (2021) (Perpendicular to the substrate plane)	0.82 / 0.79	Reported here
	Perez-Taborda, J.A., et al. (2017) (measured with this technique)	0.80	[13]
	Gahtori, B., et al. (2015) Nano Cu_2Se / Bulk Cu_2Se	0.75 / 2.7	[14]
	Liu, H., et al. (2012) Bulk	1	[15]
Ag_2Se	This work (2021) $Ag_{2-x}Se$ (Perpendicular to the substrate plane)	0.69 / 0.63	Reported here
	Jood, P., et al. (2020) Bulk	1.2	[16]
	Ding, Y., et al. (2019)	0.45	[17]
	Perez-Taborda, J.A., et al. (2018) (measured with this technique)	0.64	[18]
	Day, T., et al. (2013) $Ag_{2+x}Se$ Bulk	1.5	[19]

S.I.8. Crystallite size of bismuth telluride sample

The bismuth telluride sample is a film highly oriented in the [1 1 0] direction. See Figure S.I.7 and Table S.I.4 for the data to determine the crystallite size (D) from XRD peak with the Debye Scherrer expression in equation S.I.9:

$$D = \frac{K\lambda}{\beta cos\theta} \quad \text{(S.I.9)}$$

, where D is the average crystallite size, K is the Scherrer constant (0.93), λ is the X-ray wavelength CuKα=1.5406 $\times 10^{-10}$ m, β is ~0.007 the line broadening at FWHM in radians, and θ is 0.71 the Bragg's angle in degrees. We determine a crystalline size of 27 nm in this sample.

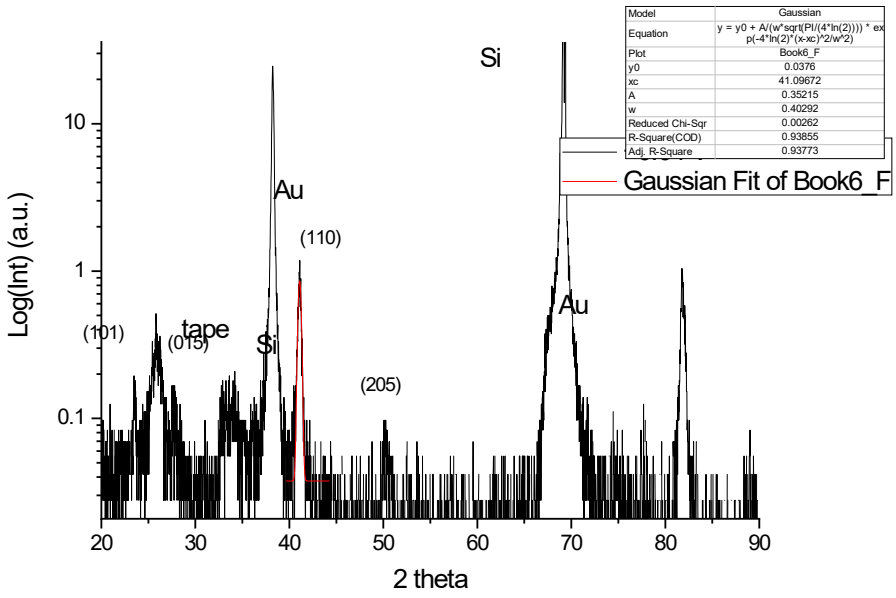

Figure S.I.7: XRD of bismuth telluride film analyzed in this experiment. The peak (1 1 0) was used to determine the crystallite size with the Debye Scherrer equation.

Table S.I.4: Data used to determine the crystallite size of bismuth telluride sample by Debye Scherrer equation with XRD of Figure S.I.7

$D = \frac{K\lambda}{\beta cos\theta}$	Values
K	9.30E-01
λ	1.54E-10
β	0.007032281
θ	0.717272727
Crystallite size	2.70601E-08

S.I.9. Sensitivity analysis of calibration curves of the equivalent resistances

In Figure S.I.8, we add a gray shadow and two dash lines in the two graphs of calibration curves for equivalent resistance, in which the sensitivity of this method is valid. However, these curves can be invalid for samples that present a critical $V_{3\omega}$ change due to high thermal conductivity samples. The change will be critical when it gives an equivalent thermal resistance out of range (out of the portion of the curve between the dash lines) or lower than the thermal contact resistance determined with the cross-point (gray shadow in the curve). In this case, the values are in a prohibited region of the curve, and the calibration parameters are not valid to determine the thermal conductivity (high values) in this case. Future work can analyze the effect of samples with high thermal conductivity values in the cross-point method, to see if the thermal contact resistance can be adjusted for the case of lower values of $V_{3\omega}$ response (for high thermal conductivity samples).

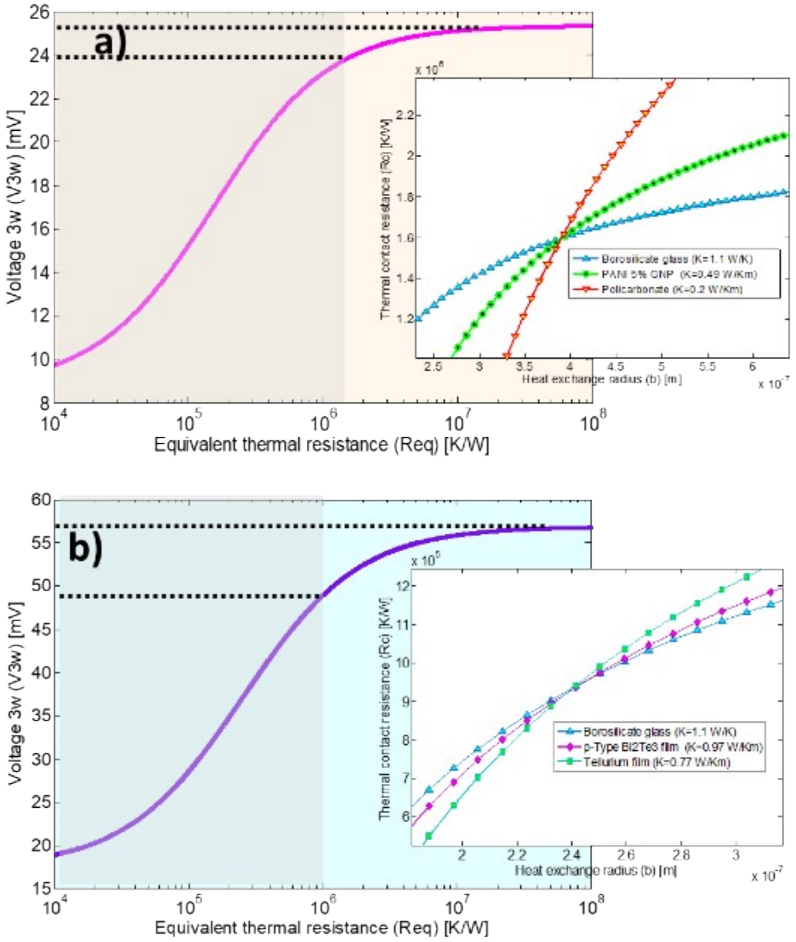

Figure S.I.8: Sensitivity analysis for curves of the equivalent resistance *vs*. $V_{3\omega}$. The prohibited region in grey shadow and the allowed voltages change between the dash lines, in which the thermal sample resistance is a positive value ($R_{eq} = R_c + R_s$).

References

1. S. Lefèvre and S. Volz, *Review of scientific instruments*, 2005, **76**, 033701.
2. E. Puyoo, S. Grauby, J.-M. Rampnoux, E. Rouvière and S. Dilhaire, *Journal of Applied Physics*, 2011, **109**, 024302.
3. T. Borca-Tasciuc, *Annual Review of Heat Transfer*, 2013, **16**.
4. C. Dames and G. Chen, *Review of Scientific Instruments*, 2005, **76**, 124902.
5. J. A. Perez-Taborda, M. M. Rojo, J. Maiz, N. Neophytou and M. Martin-Gonzalez, *Scientific reports*, 2016, **6**, 32778.
6. S. Gomès, A. Assy and P. O. Chapuis, *physica status solidi (a)*, 2015, **212**, 477-494.
7. T. Kurokawa, R. Mori, O. Norimasa, T. Chiba, R. Eguchi and M. Takashiri, *Vacuum*, 2020, **179**, 109535.
8. C. V. Manzano, B. Abad, M. M. Rojo, Y. R. Koh, S. L. Hodson, A. M. L. Martinez, X. Xu, A. Shakouri, T. D. Sands and T. Borca-Tasciuc, *Scientific reports*, 2016, **6**, 19129.
9. L. Goncalves, C. Couto, P. Alpuim, A. G. Rolo, F. Völklein and J. Correia, *Thin Solid Films*, 2010, **518**, 2816-2821.
10. H. Obara, S. Higomo, M. Ohta, A. Yamamoto, K. Ueno and T. Iida, *Japanese Journal of Applied Physics*, 2009, **48**, 085506.

11. J. Fleurial, L. Gailliard, R. Triboulet, H. Scherrer and S. Scherrer, *Journal of Physics and Chemistry of Solids*, 1988, **49**, 1237-1247.
12. H. Goldsmid, *Proceedings of the Physical Society. Section B*, 1956, **69**, 203.
13. J. A. Perez-Taborda, L. Vera, O. Caballero-Calero, E. O. Lopez, J. J. Romero, D. G. Stroppa, F. Briones and M. Martin-Gonzalez, *Advanced Materials Technologies*, 2017, **2**, 1700012.
14. B. Gahtori, S. Bathula, K. Tyagi, M. Jayasimhadri, A. Srivastava, S. Singh, R. Budhani and A. Dhar, *Nano Energy*, 2015, **13**, 36-46.
15. H. Liu, X. Shi, F. Xu, L. Zhang, W. Zhang, L. Chen, Q. Li, C. Uher, T. Day and G. J. Snyder, *Nature materials*, 2012, **11**, 422-425.
16. P. Jood, R. Chetty and M. Ohta, *Journal of Materials Chemistry A*, 2020, **8**, 13024-13037.
17. Y. Ding, Y. Qiu, K. Cai, Q. Yao, S. Chen, L. Chen and J. He, *Nature communications*, 2019, **10**, 1-7.
18. J. A. Perez-Taborda, O. Caballero-Calero, L. Vera-Londono, F. Briones and M. Martin-Gonzalez, *Advanced Energy Materials*, 2018, **8**, 1702024.
19. T. Day, F. Drymiotis, T. Zhang, D. Rhodes, X. Shi, L. Chen and G. J. Snyder, *Journal of Materials Chemistry C*, 2013, **1**, 7568-7573.
20. H.-S. Kim, Z. M. Gibbs, Y. Tang, H. Wang and G. J. Snyder, *APL materials*, 2015, **3**, 041506.